Journal of Magnetic Resonance 212 (2011) 133–138

Contents lists available at ScienceDirect

Journal of Magnetic Resonance

journal homepage: www.elsevier.com/locate/jmr

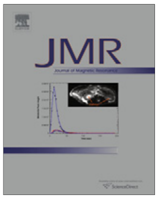

Quantitative measurements of injections into porous media with contrast based MRI

J.L. Paulsen **, M.H. Donaldson, S.S. Betancourt, Y.-Q. Song *

Schlumberger-Doll Research, One Hampshire St., Cambridge, MA 02144, USA

ARTICLE INFO

Article history:
Received 18 March 2011
Revised 17 June 2011
Available online 1 July 2011

Keywords:
Porous flow imaging
Paramagnetic tracers
Injection flow

ABSTRACT

Porous flow occurs in a wide range of materials and applies to many commercially relevant applications such as oil recovery, chemical reactors and contaminant transport in soils. Typically, breakthrough and pressure curves of column floods are used in the laboratory characterization of these materials. These characterization methods lack the detail to easily and unambiguously resolve flow mechanisms with similar effects at the core scale that can dominate at the aquifer or oil field scale, as well as the effects of geometry that control the flow at interfaces as in a perforated well or the inlet of an improperly designed column. Non-invasive imaging techniques such as MRI have been shown to provide a far more detailed characterization of the properties of the solid matrix and flow, but usually focus on the intrinsic flow properties of porous media or matching a numerical model to a complex flow system. We show that these MRI techniques, utilizing paramagnetic tagging in combination with a carefully controlled and ideal flow system, can quantitatively characterize the effects of geometry and intrinsic flow properties for a point injection into a core. The use of a carefully controlled and 'idealized' system is essential to be able to isolate and match predicted effects from geometry and extract subtle flow processes omitted in the model that would be hidden in a more heterogeneous system. This approach provides not only a tool to understand the behavior of intentional boundary effects, but also one to diagnose the unintentional ones that often degrade the data from routine column flood measurements.

1. Introduction

Laboratory flow experiments are used to characterize and understand flows in porous media applicable to many applications such as oil recovery [1], catalyst beds [2–4] and contaminant and water transport in soil [5–7]. Such porous flows can occur in a wide variety of different porous structures and environmental conditions.

To characterize the intrinsic transport properties of porous media, flow experiments are often designed to yield an effectively one-dimensional plug flow that is more amenable to analysis and interpretation. However, these interpretations necessarily rely on simplified models of column flow. Assumptions on the absence of heterogeneity and on the relevant flow mechanisms can create subtle differences in outlet composition and pressure profiles at the laboratory scale that can possibly be amplified when scaled over an aquifer or oil field. Furthermore, seemingly minor changes to the interface of the flow into a porous material can significantly alter flow properties. In laboratory one-dimensional flows, small errors in the end plates can greatly affect the flow front and interfere with interpretation, obscuring the often more subtle dispersion effects from the intrinsic structure porous media [8]. At the other extreme, flow into a perforated well will transition from spanning the expanse of the formation to the small fractures and openings at the well bore, where minor differences in the interface between the well bore and formation will influence the behavior of the overall flow [9–11].

Within this paper, we demonstrate a contrast agent based MRI technique to quantitatively study boundary dominated flows and to test and identify the relevant flow model. By carefully controlling the flow conditions and flood geometry, a good match to an analytically tractable prediction is possible, and the MRI of such a flow can help confirm and further refine the system's description. In the case of analyzing boundary dominated flows, attention to setup is especially important as subtle changes in the inlet can have a major effect on the flow front, and are easy to miss from analyzing the outflow and the pressure response of the column. Gaps, bubbles and other heterogeneities in inlet permeability will effectively short circuit or block portions of inlet flow, and small density differences in a gap will cause invading and saturating fluids to settle. Such faults are amplified and set in the shape of the flow front and will often remain even after the flow has equilibrated from inlet effects, so considerable care is necessary to reproduce the assumed boundary and initial conditions adequately. A significant amount of prior MRI work has been used to

---

* Corresponding author.
** Principal corresponding author.
E-mail addresses: jpaulsen2@slb.com (J.L. Paulsen), MDonaldson@slb.com (M.H. Donaldson), SBetancourt@slb.com (S.S. Betancourt), ysong@slb.com (Y.-Q. Song).

1090-7807/$ - see front matter © 2011 Elsevier Inc. All rights reserved.
doi:10.1016/j.jmr.2011.06.025

analyze more heterogeneous systems and numerically simulate and match the observed flow, for instance [12]. The major advantage of using a near ideal system is that subtle experimental deviations in flow can be readily identified and characterized that could otherwise either be ambiguously attributed to multiple possible causes, obscured by complex flow behavior or lost in fitting for a numerical model of the core.

Our particular use of an MRI contrast agent approach is fairly conventional and is implemented by the addition of a paramagnetic tracer such as a salt of copper, nickel, gadolinium, to either the invading or saturating fluid volume to reduce the T_1 of the tagged fluid. These tracers can be made visible under most any standard MRI sequence by reducing the recycle delay or the inclusion of a saturation pulse, and will tag the fluid at considerably less expense than a deuterated fluid and without the relatively large density difference to water [13]. As such, paramagnetic tracers have been used in the MRI imaging of porous flows to understand the motion of heavy metal contaminants [14], measure diffusion within rock cores [13,15], image flow patterns in soil cores [16], and label fluid volumes or phases within core floods [17]. What we demonstrate within this paper is that these techniques can yield quantitative agreement with flow theory in complex geometries and identify relevant transport mechanisms omitted in the theory and hence quantitatively identify unintentional boundary effects in column design, with the example of a miscible point injection flow into a Bentheimer core.

2. Flow geometry and theory

For the example system, we imaged flow in a point injection geometry, where fluid is injected through a point in an otherwise flat impermeable face. This geometry yields a simple but multidimensional flow and bares relevance in terms of fluid sampling and injection tests. By symmetry, a point injection into an infinitely large homogeneous porous medium will produce a hemispherical flow front from the injection point where the flow velocity is proportional to the inverse square of the distance. The finite size of the flow cell and the injection port will perturb this idealized flow pattern so that exact hemispherical flow only occurs at distances small relative to the total size of the system yet large relative to the size of the injection hole. With a simple outer boundary and a sufficiently small injection hole, the effect of the former can still be analytically determined, while the effect of the latter may be made experimentally negligible.

The flow cell consists of a cylindrical core with a centered injection hole on one face otherwise sealed with a rubber gasket. The remaining faces are covered by the saturating fluid in a ~1 mm gap that is directly connected to the outlet. On the face opposite of the injection hole, this free fluid is approximated by a grooved face that presses against and holds the core in position as illustrated in Fig. 1a.i. Assuming our core is uniform and the flow within it obeys Darcy's Law, the interstitial flow velocity is proportional to the pressure gradient while the pressure obeys Laplace's equation.

$$\vec{v} = -\left(\frac{\kappa}{\mu\phi}\right)\nabla p, \tag{1a}$$

$$\nabla^2 p = 0, \tag{1b}$$

The proportionality between the interstitial (pore) velocity and pressure gradient is controlled by the resistance of the porous material to flow within it (the permeability κ) the invading fluids resistance to flow (the viscosity μ), and the fraction of the volume occupied by the fluid (the porosity ϕ).

The sealed injection face prevents any flow through the surface except at the injection port. Therefore the component of the pressure gradient perpendicular to the surface is zero everywhere except for the injection port where the total flux must account for the entire flow. We approximate this point flow as uniform and take the infinitesimal limit. As the true flow profile across the injector is not uniform and occupies a finite radius, this model is invalid within the immediate vicinity of the injection hole (3–5× the injector's radius). The remaining faces are against the free saturating fluid which presents a constant pressure boundary. Due to the large contrast in permeability between the core and the surrounding free fluid, any pressure drops in this surrounding region should be negligible. Low pressures that do not change allow the

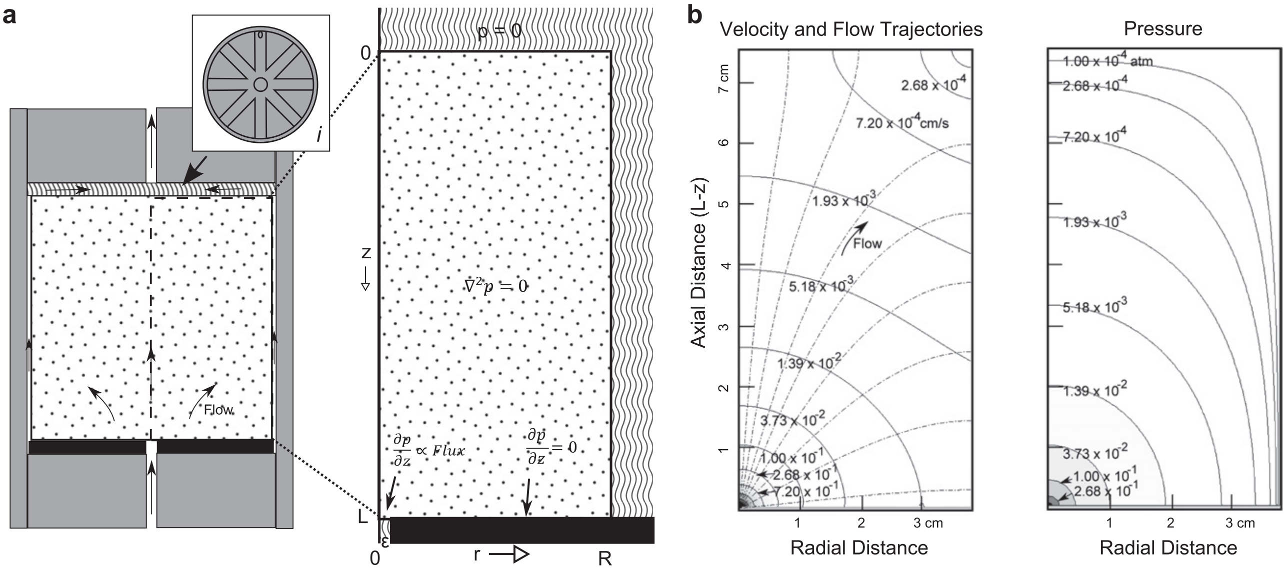

Fig. 1. a: Core holder and flow model. A rubber disk (black) presses against the core to allow flow only through the injection hole. Opposite, the surface (i) contains a star pattern of groves to press against the core while still approximating a constant pressure boundary condition for the saturating fluid. There is a gap between the surface of the core and the inside surface of the holder for a constant pressure boundary on this surface. The relevant equations, boundary conditions, and variables for the theoretical description are labeled in the adjacent diagram. 1b: Predicted pressure profile and flow velocities for our injection geometry given a 10 cc/min flow rate, 24% porosity, and 2000 mD permeability.

use of pressure gauge relative to the surrounding fluid, which is set arbitrarily at zero. Hence we can describe the boundaries as

$$\frac{\partial p}{\partial z} = \begin{cases} -\frac{c}{\pi\epsilon^2}, & \text{if } 0 < r < \epsilon \\ 0, & \text{if } \epsilon < r < R \end{cases}, \tag{2a}$$

$$p(R,z) = p(r,0) = 0, \tag{2b}$$

where the radius and length of the cylinder are R and L respectively (with the injection point at $r = 0$, $z = L$), ϵ is a vanishingly small distance and c is a constant that is determined by the total flow rate Q. In the limit $\epsilon \to 0$, the pressure may be solved as sum of terms each consisting of the product of a Bessel function over the radial dimension and a hyperbolic function over the length as detailed in the appendix.

This series solution can be converted into a velocity map by differentiation to then numerically calculate the flow paths within this geometry. However, a strict solution of the flow paths from the velocity field, as done here, will neglect the effect of dispersion on the two fluids and tracer that will be present in any flow. We selected Matlab's (ode15s) to solve for the flow paths because this velocity field represents a stiff differential equation and other built-in solvers yielded unrealistic or unstable solutions as the tracer neared the injection port. However, tracer motion still cannot be accurately calculated in the immediate vicinity of the point injection port or rubber plate, as the individual terms of the series solution diverge along this plane.

Fig. 1b plots the resulting pressure and velocity profile for our specific system: a 10 cc/min flow in a 3 in. diameter 3 in. long Bentheimer core with 24% porosity with the exact series solutions in the appendix. As expected, near hemispherical flow is apparent in both the pressure and velocity profiles and flow trajectories near the point source and deviates from hemispherical flow nearing the cores boundary. Flow fronts are shown in the comparison to the experimental data in Fig. 2.

3. Results and discussion

We apply our approach to the two possible flow fronts for the flow system (Fig. 2a and b). As detailed in the experimental section, for each experiment we monitor the flow with a slice selective spin-echo imaging sequence with either the invading or saturating fluid tagged with ~300 ppm copper(II) sulfate and stop the 10 ml/min flow for each acquisition to avoid blurring, and calibrate the intensity of each image based on the initially saturated core. Without these image adjustments (Fig. 2c), the labeled fluids are still clearly differentiated and the processing is to quantify the flow and emphasize the relevant contrast to noise. Initial vacuum saturation of the core and clearing of the injection volume with the invading fluid are essential for full saturation and reproducible flow fronts.

The 'forward' flow shown in Fig. 2a has the flow front start at the point injection port and push inwards to yield a hemispherical flow front that broadens along the radius as it nears the core's edge. The pressure profile for this geometry is perturbed from an ideal hemispherical profile as the pressure must be constant along a finite cylindrical surface corresponding to its boundary. Thus, for the fixed pressure drop, the flow traverses the shortest distance to the near corner causing faster flow along these paths broadening the flow front. Similarly, the flow path towards the far corners of the core must travel the furthest distance while the paths to the opposite end of the core to an intermediate distance corresponding to the slowest and intermediate speeds further contributing to this broadening (Fig. 1b).

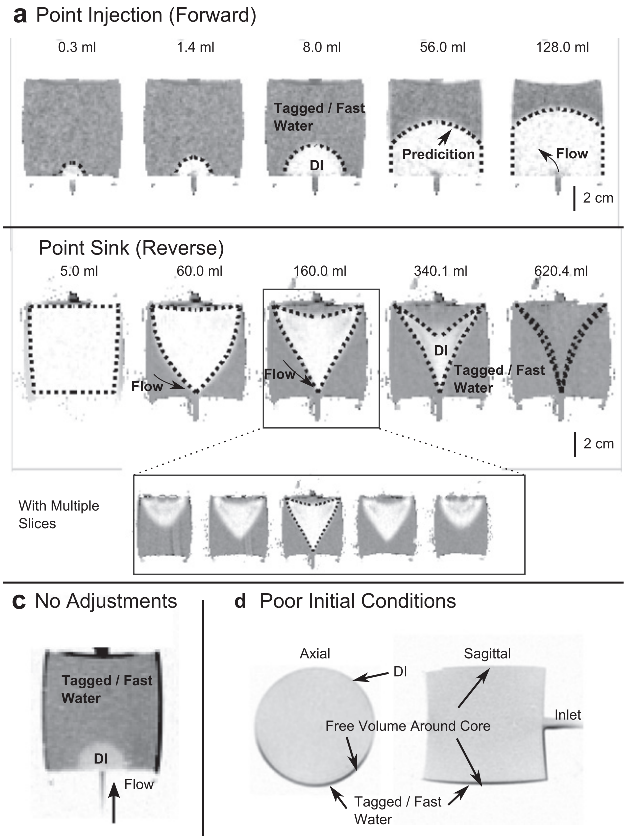

Fig. 2. T_1 weighted MRI images of the invasion fronts over a two-dimensional vertical slice along the core's axis with the end containing the outlet tubing (top) cropped. a: The point injection where fluid enters the core through the point source and b: the point sink flow where fluid exits through it for a selection of five flow volumes. These images are calibrated such that white and dark gray correspond to the core fully saturated with deionized and copper sulfate doped water respectively, and the predicted flow profiles are superimposed as dotted lines. c: Example image without calibration showing that the fluids are still clearly differentiated. d: T_1 weighted images of an improperly setup flow cell where the surrounding saturating fluid was not fully flushed and floated to the top of the flow cell.

The other flow front arises from the reverse flow. The boundary conditions for this problem are identical to the forward flow, with c having opposite sign, hence pressure and flow trajectories are identical to those shown in Fig. 1b, but the sign is reversed as we reference the differential pressure to 0 for the outer boundary. Fig. 2b shows images of the flow fronts as the invading fluid enters from the outer boundary of the core. Here, the effects of the slow flow paths are exaggerated since the variations in flow rates are greatest near the core's edges, where the hemispherical flow approximation completely breaks down. This flow leaves a succession of triangular shapes, where the flow trajectories are cleared in the order of velocity. First the outer edges clear (where the flow velocity is fastest) creating a triangle, and then the face opposite the outlet clears to hollow the triangle. The diagonal flow paths from the corners are the last to clear where the flow rates are orders of magnitude lower than elsewhere along the starting outer boundary (Fig. 1b), where flow dispersion with adjacent faster flow paths likely accelerate the clearing process.

Within both the forward and reverse flows, flow fronts appear sharp and match well with the predicted flow front indicated by the superimposed lines. Hence, the implementation and the theoretical model match at a qualitative level. A 1D projection across these two-dimensional slices provides a more quantitative comparison of these flows (Fig. 3a and b). Both forward and reverse flows follow the prediction reasonably well, but the curves are still clearly biased from the predicted profiles. These biases arise from

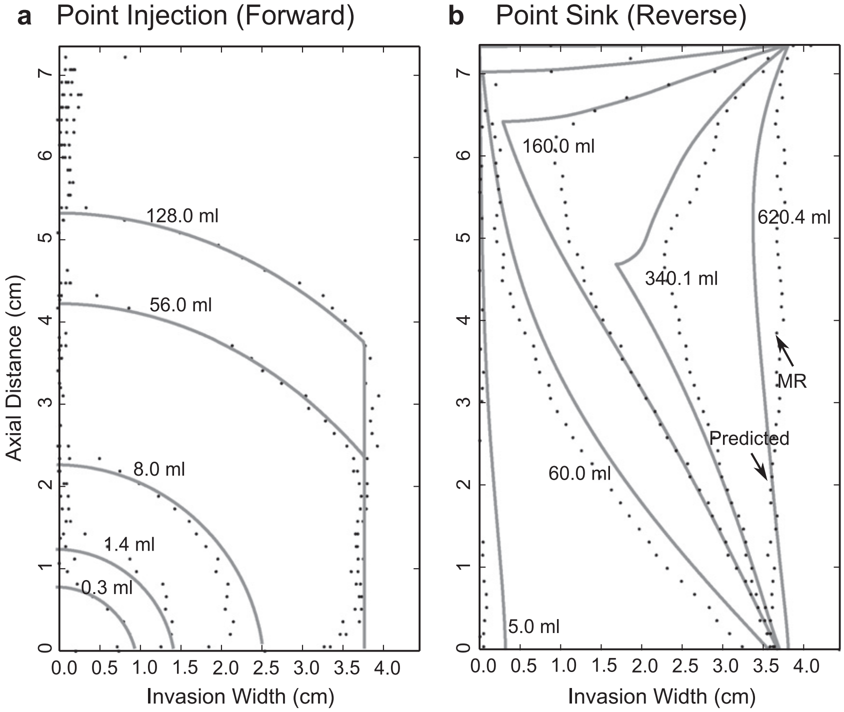

Fig. 3. One dimensional view of the flow for the a: point injection (forward) and b: point sink (reverse) flows for a quantitative comparison of the flow pattern. The one-dimensional view (dotted line) is obtained by integrating the absolute value of the signal across a centered slice running along the axis of the core but omitting signal from outside of the core, essentially producing a 1-dimensional projection along the direction of flow. This method incorporates some noise from the measurement, which is particularly evident around $r = 0$ early in the invasion in (a). We superimpose the predicted profile (solid gray lines) for comparison. Significant deviations are observed for the forward injection flow a: near the injection port where errors in the initial setup are amplified. For the reverse flow b: a similar issue near the point injection port is also observed and due to dispersion the sharp cusp predicted by theory is smoothed over.

imperfections in the initial conditions and omission of dispersive effects from the model.

Imperfections in the initial conditions arise from inadequate clearing of the fluid volume of the saturating fluid in the acting injector. For the forward point injection flow, deviations are concentrated close to the injection port where the initial flushing cleared some of the fluid in the core. These errors are further aggravated by the large difference in signal intensity between bulk fluid in the injector and saturating fluid in the adjacent core. Similarly, for the reverse flow at early times, the front is not sharp and forms a slight gradient at early times (Fig. 2b, 5 ml) due to the residual saturating water surrounding the core at the start of the experiment evident as a lowered 1D profile. This is even after considerable care was taken to fully clear the surrounding water as an abbreviated procedure (Fig. 2d) will yield a major vertical asymmetry due to the doped water settling despite the small difference in density. At later volumes, the initial gradient has been flushed from the core. However, dispersion now smooths out the expected cusp and lifts the 1D profile by partially invading the center region that would otherwise be unaffected. Returning to the full image (Fig. 2b), it is apparent that this region is partially invaded and shrunk at the far narrow corners. For a macroscopically heterogeneous core, many of these effects in either the initial conditions or the omission of dispersion in the model would be overwhelmed.

The omission of dispersion in our underlying flow model decreases its accuracy by altering the shape of the flow front, while its inclusion would greatly complicate it. The effects of dispersion can be minimized by making the self-diffusion time of the fluid negligible, but some flow dispersion is a result of flow heterogeneities at the microscopic scale present in any porous medium [18] including a homogeneous media such as a bead pack [19]. As an independent control, we monitor dispersion in the core after a rapid partial reverse flow following it over the course of a day (Fig. 4). Even immediately after the initial injection, 50% of the signal change spans around 3 mm. This initial dispersion likely accounts for the systematic errors observed in the 1D profile of the reverse flow at later times (Fig. 3). In part, this broadening arises from the slice thickness (1 mm), but radial asymmetries do not appear to be a factor as the drop occupies 2–4, 1 mm voxels before the radial averaging. After an additional 2.6 h, diffusion then leads to an additional 2 mm broadening, consistent with a 2.5 mm diffusion length expected for copper ions $\left(D_\infty = 1.4 \times 10^{-9}\ \mathrm{m^2/s}\right)$ in a 24% porous media with a formation factor[1] n of 2. By carefully controlling the flow system, the experimental results highlight the next most significant flow effect for study, in this case diffusion. This is a weakness only to the extent that it obscures other subtle effects that may arise from the geometry or heterogeneity of the flow system that are blurred by dispersion. While beyond the scope of this study, these effects could be observed directly through tracer concentration mapping as in [20] or the progress of a particular concentration contour by nulling as in [13].

No effect of using a tracer, instead of strictly monitoring the invading fluid, was observed except for a slower rate of tracer self diffusion compared to the diffusion of the bulk fluid, as observed in the long time experiment. The excellent match between the theory and MRI images and the reasonable match to the 1D profiles confirms that the $CuSO_4$ tracer can be expected to follow the bulk flow. This is not guaranteed even in a perfectly constructed flow system, as the experiment follows the motion of the paramagnetic solute and not the bulk flow. Good experimental agreement with theoretical data was only achieved by selecting the flow conditions to minimize relative tracer dispersion. This requires minimizing diffusion time to allow the tracer to follow the fluid, saturating with

---

[1] $D_\infty \approx D_0\phi^{n-1}$.

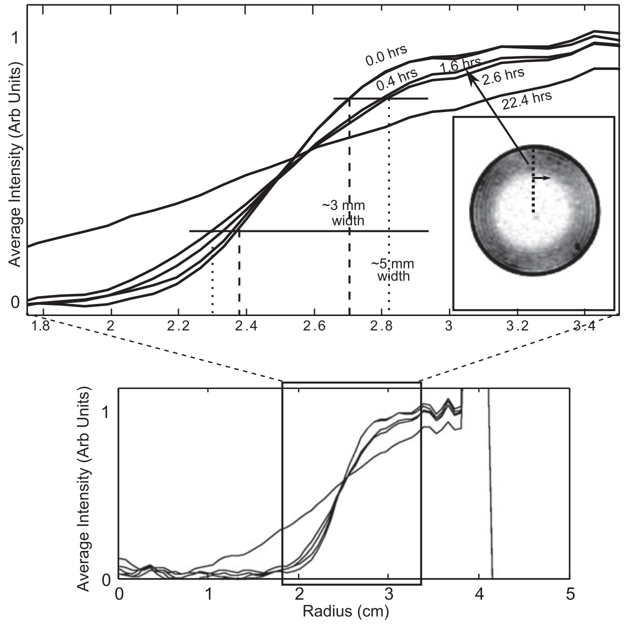

Fig. 4. Long time diffusion of the copper tracer within an axial slice of the core after an incomplete reverse flow experiment. The one 1D plot shows the average radial intensity profile for each time, linearly scaled between 0 (non-invaded) to 1 (invaded). Between flow dispersion, the 1 mm slice thickness, and imperfections in the radial averaging, immediately after the initial injection, it takes over 5 mm for the signal to ramp from its unaltered to fully invaded states. Nonetheless thresholding within a reasonable range sets the boundary region to 3 mm (i). Within 0.4 h, negligible diffusion is observed whereas after 2.6 h the boundary blurs an additional 2 mm consistent with diffusion of copper ions is at 24% porosity rock.

slightly acidic deionized water to prevent the precipitation of copper hydroxide and the selection of an inert low clay sandstone, Bentheimer, to minimize the chance of reactions with the matrix. Alternatively, different tracers, such as manganese chloride or gadolinium DPTA, or even NP contrast agents can offer chemical stability over different ranges of conditions.

In comparison to other techniques for observing slow flows in porous media, paramagnetic tagging with MRI offers several major advantages. These tracers are significantly cheaper than D_2O and have a far smaller density difference to undoped water which can greatly complicate the fluid dynamics [21,22]. Alternative MRI approaches not involving paramagnetic tracers, such as measuring the flow with spin tagging [23] and phase encoded velocimetry [18] are not appropriate for flows with fronts moving slower than ~0.1 mm/s, while alternatives outside of MRI such as X-ray CT requires heavy doping with a high Z salt [24–26] and optical techniques require precise matching of the optical properties of all components [27,28].

4. Conclusions

Many different MRI techniques have been previously applied to study porous flows as they can non-invasively yield detail of porous flows not possible with traditional flood experiments. For the case of boundary dominated flows, this is essential as the effect of flood geometry is not unambiguously distinguished with other possible retention effects with respect to tracer breakthrough or pressure response. Our experimental approach combines MRI utilizing a paramagnetic label and conventional spin echo imaging with a well controlled and characterized flow system that is yet relevant. Hence, for our example of a modified point injection, the prediction is able to closely match the observed flow were variations in the flow model, in our case the omission of dispersion, and flaws in the setup can be unambiguously identified and analyzed. While this approach is useful to examine intentional geometric effects as in our model point injection geometry, it could also be used to refine flow models or serve as an unambiguous diagnostic of column floods where the flow front shape is often implied through the shape of a breakthrough curve. Though paramagnetic tagging is limited to situations where the motion of the solute accurately follows the bulk flow, this can be ensured with careful setup and is considerably cheaper than D_2O with a far smaller chance of complications from density driven flows.

5. Experimental

5.1. Core and fluid preparation

Bentheimer sandstone typically has a very high permeability and homogeneity which makes it particularly suited to this study as an 'ideal uniform porous material.' Because of these properties, these sandstones have been used in previous MRI studies of flow through porous media, for example [29–31]. Bentheimer is very homogenous, and during the course of the study, multiple cores from the same block were used with indistinguishable results.

The Bentheimer cores are each cleaned with a series of soxhlet extractions with toluene, methanol, then chloroform. Their saturation consists of oven drying at 110 °C, degassing in a 30 mmHg vacuum, and a final immersion in the saturating fluid while still under vacuum. Each of the saturation steps last for at least an hour, a relatively abbreviated time possible due to the core's high permeability and porosity. Once in the core holder, a clean and repeatable flow front requires that either the injection port for forward flow, or the fluid surrounding the core for the reverse flow, be flushed with the invading fluid. The injection port is flushed with a blunt syringe allowing overflow through the inlet to the port. The outer chamber is flushed with a 10 ml/min flow into the main outlet port and out through another vent while rotating the cell by hand.

The invading and initially saturating fluids are differentiated by the presence or absence of copper(II) sulfate in deionized water serving as a T_1 or positive contrast agent. It is added at a relatively low concentration, 0.3 g/l, to minimize possible complications due to density differences, viscosity differences [32], solubility and ionic strength to the point that they are experimentally negligible. Paramagnetic tracers such as a manganese salt or Gd-DTPA would be equally viable depending on their stability in solution. Care was taken to avoid even slightly alkaline conditions as copper(II) hydroxide is sparsely soluble.

5.2. MRI

All MRI experiments are performed in a 2 T horizontal magnet with a 180 mm ID, 10 G/cm Gradient set and a 125 mm ID birdcage RF coil. The images are collected as a multi-slice multi-echo imaging experiment with 1.5 mm slices, 1.5 mm in plane resolution and a 8.7 ms echo time. A short repetition delay (500 ms) generates the T_1 contrast, and relies on the previous echo train for saturation. A spin echo sequence and a moderately high acquisition band width (50 kHz) are necessary due to the inherently broad linewidth of the saturated rock core from the internal gradients generated by the susceptibility mismatch between saturating fluid and rock. Alternatively single point techniques such as SPI or SPRITE [33] could provide more robust imaging modalities compatible with T_1-relaxation agents at the possible expense of experiment time. The total acquisition time of each scan is 2 min and 8 s.

The images are processed in Matlab and are all first adjusted by a mild Gaussian filtering. The final contrast-only images are adjusted for variations in coil sensitivity by defining the signal range at each voxel by its DI and tagged fluid saturated values as 0 and 1 respectively. The reference calibration values are based on images obtained before and after each flow experiment. Overall, this processed signal gives the quantity of invaded fluid in each voxel assuming minimal mixing and diffusion of the tracer between the two phases.

Acknowledgments

We would like to thank Schlumberger for allowing us to publish this research and many of our colleagues here at the Schlumberger-Doll Research center for their general advice and support. In particular, Wave Smith and Lisa Meeks for assistance with core preparation and Elizabeth B. Dussan V. and T.S. Ramakrishnan for their discussions on the fluid mechanics.

Appendix A. Series solution to the injection flow

The solution to Darcy's Law for our particular geometry may be solved as a series solution consisting of the product of Bessel functions along the radial dimension and hyperbolic functions along the axial. With the constant pressure boundary condition set to 0, the viable eigenvalues are the roots of the Bessel function, β_n, and the requirement of a finite pressure restricts us to J_0. The constant pressure boundary condition at the far end, defined at $z = 0$, restricts the solution to sinh functions along the axial direction. Finally, the boundary condition for the injection port determines the remaining coefficients to the series solution. Hence

$$p = \sum_{n=1}^{\infty} A_n J_0\left(\frac{\beta_n}{R} r\right) \sinh\left(\frac{\beta_n}{R} z\right), \tag{A.1}$$

$$\hat{u} = -\frac{k}{\mu}\nabla p, \tag{A.2}$$

where

$$A_n = -\frac{\mu Q}{k}\left[\pi R \beta_n \cosh\left(\frac{\beta_n}{R} L\right) J_1^2(\beta_n)\right]^{-1}, \tag{A.3}$$

$$\frac{\partial p}{\partial r} = \sum_{n=1}^{\infty} -A_n \frac{\beta_n}{R} J_1\left(\frac{\beta_n}{R} r\right) \sinh\left(\frac{\beta_n}{R} z\right), \tag{A.4}$$

$$\frac{\partial p}{\partial z} = \sum_{n=1}^{\infty} A_n \frac{\beta_n}{R} J_1\left(\frac{\beta_n}{R} r\right) \cosh\left(\frac{\beta_n}{R} z\right). \tag{A.5}$$

which we evaluate over the valid region $0 < z < L$ and $0 \leqslant r \leqslant R$. Because of the approximation of a point source (sink) with uniform flow, the solution is invalid within the immediate vicinity of the injection hole to about five times the injection hole radius. For numerical computations, we precomputed the invariant coefficients for fixed L and R and then summed in reverse order the first 110 terms. The addition of further terms begins to introduce numerical errors into the solution due to the rapid increase in the values of $\cosh\left(\frac{\beta_n L}{R}\right)$ and $\sinh\left(\frac{\beta_n z}{R}\right)$ canceling imperfectly. Alternatively, these terms can be combined for better convergence. However, their separate computation only becomes important immediately near $z = L$, and does not significantly impact the flow computations otherwise.

References

[1] D. Levitt, A. Jackson, C. Heinson, L. Britton, T. Malik, V. Dwarakanath, G. Pope, Identification and evaluation of high-performance EOR surfactants, in: Proceedings of SPE/DOE Symposium on Improved Oil Recovery, 2006.

[2] M.H. Al-Dahhan, F. Larachi, M.P. Dudukovic, A. Laurent, High-pressure trickle-bed reactors: a review, Ind. Eng. Chem. Res. 36 (1997) 3292–3314.

[3] S.K. Bej, Performance evaluation of hydroprocessing catalysts: a review of experimental techniques, Energy Fuels 16 (2002) 774–784.

[4] S. Roy, T. Bauer, M. Al-Dahhan, P. Lehner, T. Turek, Monoliths as multiphase reactors: a review, AIChE J. 50 (2004) 2918–2938.

[5] L.W. Gelhar, C. Welty, K.R. Rehfeldt, A critical review of data on field-scale dispersion in aquifers, Water Resour. Res. 28 (1992) 1955.

[6] C. Shackelford, Laboratory diffusion testing for waste disposal – a review, J. Contam. Hydrol. 7 (1991) 177–217.

[7] R.P. Schwarzenbach, J. Westall, Transport of nonpolar organic compounds from surface water to groundwater. Laboratory sorption studies, Environ. Sci. Technol. 15 (1981) 1360–1367.

[8] J. Kyte, L. Rapoport, Linear waterflood behavior and end effects in water-wet porous media, J. Pet. Technol. 10 (1958).

[9] S. Tariq, M. Ichara, L. Ayestaran, Performance of perforated completions in the presence of anisotropy, laminations, or natural fractures, SPE Prod. Eng. 4 (1989) 376–384.

[10] W. Bell, E. Berieger, J.J. Harrigan, Laboratory flow characteristics of gun perforations, J. Pet. Technol. 24 (1972) 1095–1103.

[11] C.O. Karacan, A.S. Grader, P.M. Halleck, Mapping of permeability damage around perforation tunnels, J. Energy Resour. Technol. 123 (2001) 205.

[12] E. Zuluaga, P. Majors, E. Peters, A simulation approach to validate petrophysical data from NMR imaging, SPE J. 7 (2002).

[13] A.E. Fischer, B.J. Balcom, E.J. Fordham, T.A. Carpenter, L.D. Hall, A fast inversion recovery NMR imaging technique for mapping two-dimensional tracer diffusion and dispersion in heterogeneous media, J. Phys. D: Appl. Phys. 28 (1995) 384.

[14] N. Nestle, A. Wunderlich, R. Niessner, T. Baumann, Spatial and temporal observations of adsorption and remobilization of heavy metal ions in a sandy aquifer matrix using magnetic resonance imaging, Environ. Sci. Technol. 37 (2003) 3972–3977.

[15] G. Guillot, G. Kassab, J.P. Hulin, P. Rigord, Monitoring of tracer dispersion in porous media by NMR imaging, J. Phys. D: Appl. Phys. 24 (1991) 763.

[16] S. Haber-Pohlmeier, M. Bechtold, S. Stapf, A. Pohlmeier, Water flow monitored by tracer transport in natural porous media using magnetic resonance imaging, Vadose Zone J. 9 (2010) 835.

[17] B. Baldwin, W. Yamanashi, Detecting fluid movement and isolation in reservoir core with medical NMR imaging techniques, SPE Reservoir Eng. 4 (1989).

[18] J.D. Seymour, P.T. Callaghan, Generalized approach to NMR analysis of flow and dispersion in porous media, AIChE J. 43 (1997) 2096–2111.

[19] A.J. Sederman, M.L. Johns, P. Alexander, L.F. Gladden, Structure–flow correlations in packed beds, Chem. Eng. Sci. 53 (1998) 2117–2128.

[20] B.S. Akpa, S.M. Matthews, A.J. Sederman, K. Yunus, A.C. Fisher, M.L. Johns, L.F. Gladden, Study of miscible and immiscible flows in a microchannel using magnetic resonance imaging, Anal. Chem. 79 (2007) 6128–6134.

[21] K. Ilvonen, L. Palva, M. Permki, R. Joensuu, R. Sepponen, MRI-based D_2O/H_2O-contrast method to study water flow and distribution in heterogeneous systems: demonstration in wood xylem, J. Magn. Reson. 149 (2001) 36–44.

[22] A. Pohlmeier, D. van Dusschoten, L. Weihermüller, U. Schurr, H. Vereecken, Imaging water fluxes in porous media by magnetic resonance imaging using D_2O as a tracer, Magn. Reson. Imaging 27 (2009) 285–292.

[23] P. Bendel, Quantification of slow flow using FAIR, Magn. Reson. Imaging 27 (2009) 587–593.

[24] S. Wellington, H. Vinegar, CT studies of surfactant-induced CO_2 mobility control, in: Proceedings of SPE Annual Technical Conference and Exhibition, 1985.

[25] S. Wellington, H. Vinegar, X-ray computerized tomography, J. Pet. Technol. 39 (1987).

[26] H. Vinegar, X-ray CT and NMR imaging of rocks, J. Pet. Technol. 38 (1986).

[27] J.G. Santiago, S.T. Wereley, C.D. Meinhart, D.J. Beebe, R.J. Adrian, A particle image velocimetry system for microfluidics, Exp. Fluids 25 (1998) 316–319.

[28] C. Xi, D.L. Marks, D.S. Parikh, L. Raskin, S.A. Boppart, Structural and functional imaging of 3D microfluidic mixers using optical coherence tomography, Proc. Natl. Acad. Sci. U. S. A. 101 (2004) 7516–7521.

[29] D.N. Guilfoyle, P. Mansfield, K.J. Packer, Fluid flow measurement in porous media by echo-planar imaging, J. Magn. Reson. 97 (1992) 342–358.

[30] S. Sheppard, Magnetic resonance imaging study of complex fluid flow in porous media: flow patterns and quantitative saturation profiling of amphiphilic fracturing fluid displacement in sandstone cores, Magn. Reson. Imaging 21 (2003) 365–367.

[31] R. Waggoner, E. Fukushima, Velocity distribution of slow fluid flows in bentheimer sandstone: an NMRI and propagator study, Magn. Reson. Imaging 14 (1996) 1085–1091.

[32] Concentrative properties of aqueous solutions: density, refractive index, freezing point depression, and viscosity, in: W.M. Haynes, D.R. Lide (Eds.), CRC Handbook of Chemistry and Physics, CRC Press Inc., 2011, pp. 8–56.

[33] B. Blumich, NMR Imaging of Materials, Oxford University Press, Oxford, 2000.